A high-performance solar chimney in building integrated with photocatalytic technology for atmospheric methane removal

A high-performance solar chimney in building integrated with photocatalytic technology for atmospheric methane removal

Aocheng Li[1], Tingzhen Ming[1,*], Hanbing Xiong[1], Yongjia Wu[1], Tianhao Shi[1], Wei Li[2,*], Renaud de Richter[3], Yanhua Chen[4], Xiaoliang Tang[4], Yanping Yuan[5]

1. School of Civil Engineering and Architecture, Wuhan University of Technology, Wuhan 430070, China

2. Institute for Materials and Processes, School of Engineering, The University of Edinburgh, Edinburgh EH9 3FB, Scotland, UK

3. Tour-Solaire.Fr, 8 Impasse des Papillons, F34090 Montpellier, France.

4. CITIC General Institute of Architectural Design and Research CO.,Ltd, Wuhan 430014, China.

5. School of Mechanical Engineering, Southwest Jiaotong University, Chengdu 610031, China

Corresponding author:

Tingzhen Ming: School of Civil Engineering and Architecture, Wuhan University of Technology, Wuhan 430070, China. Email: tzming@whut.edu.cn

Wei Li: *Institute for Materials and Processes, School of Engineering, The University of Edinburgh, Edinburgh EH9 3FB, Scotland, UK. Email: Wei.Li@ed.ac.uk*

Abstract: The techniques for the removal of methane from the atmosphere are highly challenging due to its stable chemical properties, dispersed sources, and low concentrations. This paper proposes a practical small-scale solar chimney (SC) in buildings with photocatalytic reactors (PCRs) for atmospheric methane removal. Two comprehensive numerical models on photocatalytic reaction and indoor ventilation are developed. The numerical simulation considers the performance of methane removal and indoor air ventilation of the proposed system, as well as its specific crucial parameters such as the type of PCRs, solar radiation, and flow channel width. The obtained results show that the SC with honeycomb photocatalytic reactor (HPCR) is more able to remove atmospheric methane than SC with plate photocatalytic reactor (PPCR) under the premise of meeting the ventilation standards. In addition, there is a maximum methane purification rate of 57.27 μg/s under the condition that the air gap width is 0.3 m, the length of the HPCR is 1.5 m, and the porosity is 0.85. It is then proved that the SC in buildings with PCRs can allow small-scale, zero-energy consumption, continuable, and decentralized low-concentration atmospheric methane removal while improving the indoor ventilation.

Keywords: solar chimney in buildings, methane removal, photocatalysis, ventilation

Nomenclature

B, B_1, B_2	Constant parameters measured by experiment
C	Inertia coefficient of the honeycomb structure
$C_{1\varepsilon}$, $C_{2\varepsilon}$	Constants for turbulent model
c_1, c_2	Mole concentration of methane and oxygen, *mol/m^3*
c_p	Specific heat at constant pressure, *J/(kg·K)*
D_p	Pore diameter of the honeycomb structure, *mm*
g	Acceleration of gravity, *m/s^2*
G_k	Generic term of the turbulent kinetic energy due to mean velocity gradients, *J*

G_b	Generic term of the turbulent kinetic energy due to buoyancy, *J*
$\vec{J_i}$	Diffusion flux of species *i*, *mol/(s·m³)*
K	Permeability of the honeycomb structure
p	Pressure, *Pa*
Q_m	Mass flow rate of methane, *kg/s*
q	Heat flux, *W/m²*
R_i	Amount of component i produced or consumed in a chemical reaction
r_m	Reaction rate, $\mu g/s$
r_{AI}	Reaction rate per unit of catalyst surface and absorbed irradiation intensity, *mol/(W·s)*
S_i	Additional rate due to the discrete phase
S_Φ	Momentum loss term
S_p	Outer surface area of the honeycomb structure
SSA	Specific surface area, *m²*
T_0	Ambient temperature, *K*
u_i, u_j	Components of velocity in *i* direction and *j* direction, *m/s*
V_p	Volume of the honeycomb structure, *m³*
Y_M	Additional rate owing to the discrete phase
x, y, z	Cartesian space coordinates
Symbols	
ρ	Gas density, *kg/m³*
τ	Viscous stress tensor, *N/m²*
k	Karman Constant
β	Expansion coefficient, *1/K*
ν	Kinetic viscosity, *m²/s*
γ	Porosity of the honeycomb structure
Abbreviation	
SC	Solar chimney
PCR	Photocatalytic reactor

HPCR	Honeycomb photocatalytic reactor
PPCR	Plate photocatalytic reactor

1. Introduction

The human-induced climate change greatly increased the intensity and frequency of weather extremes, causing widespread impacts on the ecosystems. In addition, irreversible loss, including natural systems degradation and species extinction, became apparent (Pörtner et al., 2022). In recent years, events such as ocean acidification, permafrost thawing in polar regions, hydrological changes, and bushfire outbreaks frequently occurred, increasing the high vulnerability of ecosystems and humans. In light of the recent climate trends, the commitments of the Paris Agreement should be deepened to stabilize the global average temperature at 1.5℃ above pre-industrial levels (Hoegh-Guldberg et al., 2019).

To effectively implement plans for greenhouse gas reduction, transformative actions based on cutting emissions and terminal capture were used. As a greenhouse gas of great concern, carbon dioxide can be removed by afforestation and reforestation (AR) and carbon capture and storage (CCS) (Hepburn et al., 2019). However, methane, which is the second most important greenhouse gas contributing about a quarter of the global warming (Ocko et al., 2018; Ocko et al., 2021), was underappreciated. It then increasingly became studied due to its high global warming potential and short lifecycle in the atmosphere.

The Global Methane Pledge, which is the headline decision of the 26th Conference of the Parties (COP 26) to the United Nations Framework Convention on Climate Change, aimed at reducing at least 30% of the global methane emissions by 2030 compared to 2020 levels (Keramidas et al., 2021). The atmospheric methane levels have been increasing since 1975 (Saunois, M. et al., 2020). The mitigation of methane will remarkably help slowing global warming over the coming decades (Harmsen et al., 2019; Saunois et al., 2016). The methane sources in the atmosphere are mainly the

anthropogenic emissions from waste, agriculture, extraction, and utilization of fossil fuel, as well as the natural emissions from freshwater systems, wetlands, and geological resources (Ganesan et al., 2019; Jackson et al., 2020). Anthropogenic methane emissions are widespread in cities and rural areas. They contributed to 50-65% of total methane emissions over the last 30 years (Ganesan et al., 2019; Liu et al., 2021; Saunois, Marielle et al., 2020).

Techniques such as thermal catalysis (Lustemberg et al., 2018), photocatalysis (Wang et al., 2022), methanotrophic bacteria (Jeffrey et al., 2021), and direct air capture by zeolites (Jackson et al., 2019) were proposed and investigated to remove atmospheric methane. As a potential strategy for methane removal, photocatalysis uses only solar energy under mild and controllable conditions (Meng et al., 2019; Song et al., 2019). It was found that methane could be converted into CO_2 and formaldehyde under UV light (Wada et al., 1993). Further experimental study indicated that the photocatalytic reaction of methane was more active under UV radiation at wavelengths less than 310 nm, producing CH_3OH, CO_2, and H_2O. The photocatalyst was very important for the photocatalytic methane oxidation. The Ag/ZnO nanocatalyst had remarkable activity in the methane oxidation under solar irradiation, ultimately converting CH_4 at concentrations in the range of 100-10,000 ppm to CO_2 within 20-240 min (Chen et al., 2016). Li et al. (Li et al., 2019) synthesized an effective CuO/ZnO photocatalyst that can convert 100 ppm of CH_4 to CO_2 with a conversion rate greater than 90%. Other photocatalysts having high efficiency in methane oxidation exist, such as $SrCO_3/SrTiO_3$ (Pan et al., 2016), $BiVO_4$ Bipyramids (Zhu et al., 2018), and TiO_2 (P25). P25 has high chemical stability as a photocatalyst, is environmentally benign, and has a low cost, which makes it the most widely used semiconductor photocatalyst (Zhang et al., 2022).

Most of the current studies on methane photocatalysis were conducted in a laboratory setting rather than in an outdoor atmospheric environment (Ming et al., 2022). However, in the real atmospheric environment, the concentration of methane is

extremely low and its sources are dispersed, which is significantly different from laboratory conditions. Therefore, air capture devices are necessary for the capture and subsequent treatment of the atmospheric methane. A solar chimney power plant with photocatalytic reactors (SCPP-PCRs) was proposed to reduce the non-CO_2 greenhouse gases in the atmosphere, such as methane (Ming et al., 2017). It was estimated that this system can effectively mitigate the climate change by treating one atmospheric volume of non-CO_2 greenhouse gases every 14-16 years using 50,000 SCPPs with an output of 200 MW. Then, it was evaluated that the performance and influencing parameters of photocatalytic oxidation of methane by the SCPP-PCRs through numerical simulations, which demonstrated the potential of methane removal from the atmosphere on a larger scale (Ming et al., 2021; Ming et al., 2022). Through theoretical calculations, the methane removal capacity of SCPP-PCRs with different sizes, configurations, and photocatalyst types were studied (Huang et al., 2021).

However, the main obstacles to the development of the SCPP-PCRs were the enormous land area required for construction and the high investment costs. Large-scale systems are inherently well-suited for regions with widespread and high-concentration methane emissions, such as large livestock farms. However, it is equally crucial to address methane emissions originating from human activities in urban areas, particularly those arising from sources such as natural gas used in cooking processes. These emissions can lead to methane concentrations several times higher than the average atmospheric methane concentration within a short timeframes and limited geographical areas. These urban emissions are characterized by their dispersed nature and require specific attention. Hence, proposing a novel atmospheric methane removal system specifically designed for urban environments is a primary technical challenge that should be urgently solved. The system should exhibit characteristics such as proximity to emission sources, decentralization, small-scale implementation, sustainability, cost-effectiveness, and simplicity of design.

Solar chimney in buildings is a device that utilizes the solar chimney effect to

enhance indoor ventilation, sharing similarities with SCPP in principle. Both systems rely on the solar chimney effect as a driving force, enabling the capture of surrounding gases from indoor and outdoor environments. The combination of this feature with catalytic systems thus prompted the rise of some innovative systems. A novel photocatalytic-Trombe wall was proposed to degrade formaldehyde (Yu et al., 2017). Through comprehensive day-long experiments and a coupled kinetic, thermal and mass model, the system exhibited an impressive formaldehyde degradation rate of 100 $mg/m^2/day$ (Yu et al., 2018). Additionally, a numerical study investigated the integrated performance of the photocatalytic-Trombe wall solar chimney system under realistic thermal boundary conditions (Wu et al., 2020). The findings demonstrated that the air degradation rate increased and then decreased with rising solar radiation intensity. Consequently, it can be deduced from the literature that due to its flexible structure, the integration of SC in buildings and photocatalytic technologies holds great potential for capturing and removing atmospheric methane.

The PCRs have two typical types of the plate photocatalytic reactor (PPCR) and the honeycomb photocatalytic reactor (HPCR) (Xiong et al., 2022). The structural parameters of the photocatalytic reactor play a crucial role in determining the photocatalytic reaction rate, thereby directly affecting the overall photocatalytic efficiency of the system. Similarly, the geometric parameters of SC in buildings are of great importance in influencing the airflow capture and facilitating indoor ventilation (Shi et al., 2018). A mathematical model on SC in buildings found that the air flow rate exhibited an increasing trend with the increment of chimney width (Ong and Chow, 2003). Within a specific width range, tripling the chimney width could improve the ACH by more than 25% (Bassiouny and Koura, 2008). Several studies (Arce et al., 2009) (Mathur et al., 2006) have suggested that a chimney width ranging from 0.2 to 0.3 m is optimal for achieving maximum performance. The optimum value is not unfixed but dependent on other factors such as the chimney angle and the chimney height. Except for the structural parameters, solar radiation also of paramount

importance in driving the airflow within chimney-effect-driven systems and driving the photocatalytic reaction of methane. It can be affirmed that high solar radiation can enhance the performance of solar chimneys (Burek and Habeb, 2007; Shi et al., 2016).

In this paper, a practical small-scale SC in buildings with PCRs is proposed to remove the atmospheric methane and enhance the indoor ventilation. The overall performance of the proposed system and the specific crucial parameters, such as the type of PCRs, solar radiation, and flow channel width, are analyzed using a numerical method. By combining buildings and photocatalytic technologies, this study can reduce the operational energy consumption of buildings while retaining the possibility of urban-scale methane removal to mitigate the greenhouse effect.

2. Model description

2.1. Geometric model

The SC is driven by solar energy, including a glazing cover, an absorbing wall, and a flow channel. Sunlight enters through the glazing cover, and most of it is absorbed by the wall. The air in the flow channel is then heated by the high-temperature wall. The heated air floats upwards due to the buoyancy effect, and the outdoor air enters the room, allowing the indoor air ventilation of the building without energy consumption.

The SC configuration in the building with PCRs is shown in Fig. 1. The dimensions of the experimental cell are 3 m × 3 m × 3 m, which is similar to the commonly used experimental model (Bassiouny and Koura, 2008; Mathur et al., 2006; Rabani et al., 2015). The window is located at the center of the north wall with a height of 0.9 m. The chimney width is 0.3 m, connecting to the interior zone through an entrance of 0.3 m × 3 m × 0.1 m in the south wall. The SC is integrated with PCRs used for methane degradation. The PPCR and HPCR are used for the SC. Note that the P25 is coated on the surface of the absorbing wall for PPCR, and on the surface of every pore of the honeycomb pore structure for HPCR.

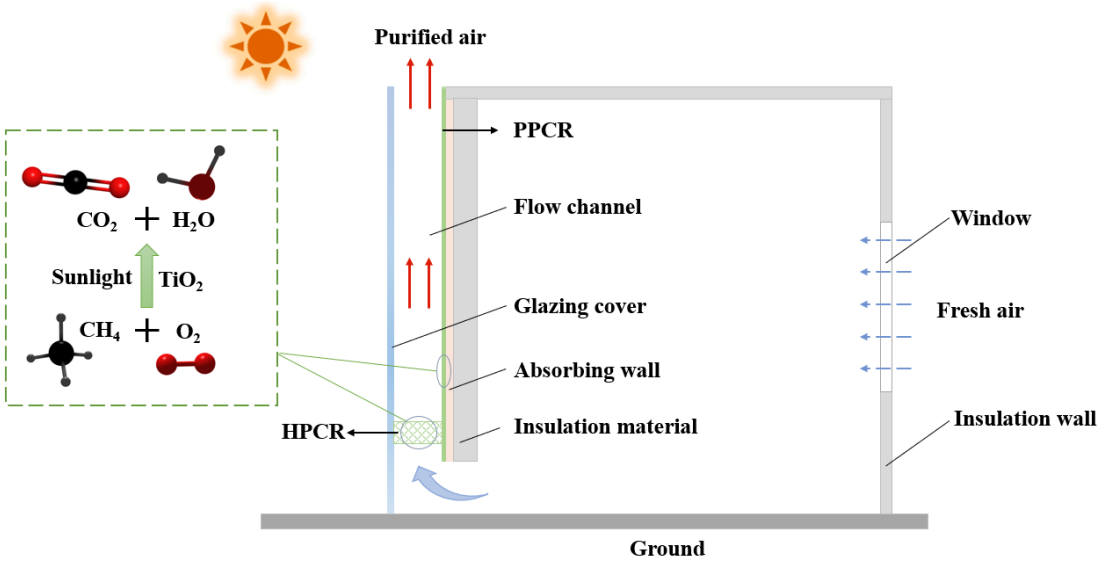

Fig.1. Schematic of the SC in the building with PCRs.

2.2. Mathematical model

The development of turbulence is insufficient in the airflow inside the flow channel. In this study, the standard *k-ε* model is used. The governing equations including the continuity, momentum, energy, standard *k-ε*, and transport equations, are given by:

Continuity equation:

$$\frac{\partial(\rho u_i)}{\partial x_i} = 0 \tag{1}$$

Momentum equation:

$$\frac{\partial(\rho u_i u_j)}{\partial x_j} = \rho g \beta (T - T_0) - \frac{\partial p}{\partial x_i} + \frac{\partial \tau_{ij}}{\partial x_j} \tag{2}$$

Energy equation:

$$\frac{\partial(\rho c_p u_j T)}{\partial x_j} = \frac{\partial}{\partial x_j}\left(\lambda \frac{\partial T}{\partial x_j}\right) - \tau_{ij}\frac{\partial u_i}{\partial x_j} + \beta T\left(\frac{\partial p}{\partial x_j} + u_j \frac{\partial p}{\partial x_j}\right) \tag{3}$$

The equation for the turbulent kinetic energy (k):

$$\frac{\partial}{\partial x_i}(\rho k u_i) = \frac{\partial}{\partial x_j}\left(\alpha_k \mu_{eff} \frac{\partial k}{\partial x_j}\right) + G_k + G_b - \rho\varepsilon - Y_M + S_k \tag{4}$$

The equation for the energy dissipation (ε):

$$\frac{\partial}{\partial x_i}(\rho \varepsilon u_i) = \frac{\partial}{\partial x_j}\left(\alpha_\varepsilon \mu_{eff} \frac{\partial \varepsilon}{\partial x_j}\right) + C_{1\varepsilon}\frac{\varepsilon}{k}(G_k + C_{3\varepsilon}G_b) - C_{2\varepsilon}\rho\frac{\varepsilon^2}{k} - R_\varepsilon + S_\varepsilon \tag{5}$$

Component transport equation:

$$\nabla \cdot (\rho \vec{v} Y_i) = -\nabla \cdot \vec{J_\iota} + R_i + S_i \quad (6)$$

where ρ is the fluid density (kg/m^3), u_i and u_j are respectively the velocity components in different directions (m/s), β is the expansion coefficient (1/K), T_0 is the ambient temperature (K), τ_{ij} is defined as $\tau_{ij} = -\rho\overline{u_i' + u_j'}$, G_k is the generic term of k due to mean velocity gradients which can be defined as $G_k = -\rho\overline{u_\iota' u_J'}\frac{\partial u_j}{\partial x_i}$, α_k is the turbulent Prandtl number for k which is defined as $\alpha_k = 1.0$, α_ε is the turbulent Prandtl number for ε which is defined as $\alpha_\varepsilon = 1.3$, G_b is the generic term for k due to buoyancy, $C_{1\varepsilon}$ and $C_{2\varepsilon}$ are two constants for the turbulent model that are defined as $C_{1\varepsilon} = 1.44$ and $C_{2\varepsilon} = 1.92$, $\vec{J_\iota}$ is the diffusion flux of species i which is defined as $\vec{J_\iota} = -\rho D_{i,m} + R_i$, R_i is the amount of component i produced or consumed in a chemical reaction, S_i is the additional rate due to the discrete phase, and Y_M denotes the contribution of incompressible turbulence of fluctuating expansion to the overall dissipation rate.

For the PPCR, Andreas et al. (Haeger et al., 2004) derived the surface reaction rate formula of photocatalysis methane oxidation:

$$r_{AI} = B\frac{B_1 c_1}{1+B_1 c_1}\frac{B_2 c_2}{1+B_2 c_2} \quad (7)$$

where r_{AI} is the surface reaction rate of the methane per absorbed irradiation intensity and unit surface, c_1 and c_2 respectively represent the concentrations of methane and oxygen, $B, B_1,$ and B_2 are the constant parameters measured in the experiment as 5.37 $\times 10^{-7}$, 2.42, and 4.60, respectively.

The HPCR can be considered as a porous medium (Mazumder and Sengupta, 2002; Ming et al., 2021). Given the Ergun equation (Wang et al., 2014), the permeability (K) and the inertia coefficient (C) of the region can be derived:

$$K = \frac{D_P^2}{150}\frac{\gamma^3}{(1-\gamma)^2} \quad (8)$$

$$C = \frac{3.5}{D_P^2}\frac{(1-\gamma)}{\gamma^3} \quad (9)$$

where γ and D_p are the porosity and the pore diameter of the reactor, respectively.

The formula for the reaction rate in the HPCR is given by:

$$r_m = r_{AI} \cdot SSA \tag{10}$$

where r_{AI} is the reaction rate per unit of catalyst surface and absorbed irradiation intensity, and SSA is the specific surface area that can be calculated as (Wang et al., 2014):

$$SSA = \frac{(1-\gamma)S_p}{V_p} = \frac{6(1-\gamma)}{\pi D_p^3}\pi D_p^2 = \frac{6(1-\gamma)}{D_P} \tag{11}$$

where S_p is the outer surface area of the honeycomb structure and V_p is the volume of the honeycomb reactor.

The HPCR is simplified as a porous media zone. The heat transfer process in the porous media is controlled by the equilibrium thermal model using the TiO_2 material. The mass conservation and the momentum conservation of the internal region are given by:

Continuity equation:

$$\nabla \cdot (\gamma\rho\vec{v}) = 0 \tag{12}$$

Momentum equation:

$$\nabla \cdot (\gamma\rho\vec{v}) = -\gamma\nabla p(\gamma\vec{\tau}) + \gamma\rho\vec{g} + S_\Phi \tag{13}$$

where $\vec{\tau}$ is the viscous stress tensor, S_Φ is the momentum loss term which consists of the viscous loss term and the inertial loss term ($S_\Phi = -(\frac{\mu}{K}\vec{v} + \frac{C}{2}\rho|\vec{v}|\vec{v})$).

The photocatalytic efficiency and purification rate of methane are expressed as:

$$\eta_{methane} = \frac{J_1 - J_2}{J_1} \tag{14}$$

$$\dot{m}_{methane} = Q_m(m_1 - m_2) \tag{15}$$

where J_1 and J_2 are respectively the methane concentration at the chimney entrance and exit, Q_m is the mass flow rate of methane, m_1 and m_2 are the mass fraction of methane at the chimney entrance and exit, respectively.

2.3. Boundary conditions

The boundary conditions set for the simualtion are presented in Table 1. The room entrance (i.e., window area) is set as a pressure inlet and the chimney outlet is set as a pressure outlet. The outdoor ambient temperature is 293 K and the convective heat

transfer coefficient between the glass and the environment can be set as 5.7 W/(m^2·K) (Wu et al., 2020). The heating of the absorbing wall by solar radiation is considered as heat flux. Considering the energy loss through convection and radiation (Wu et al., 2020; Yu et al., 2018), a discount factor of 0.71 is used. All the other surfaces of the model are set as adiabatic and non-slip walls.

Table 1 Boundary conditions

Location	Boundary type	Value
Window	Pressure inlet	p = 0 Pa, T = 293 K
Chimney outlet	Pressure outlet	p = 0 Pa
Absorbing wall	Heat flux	q = 300 – 1100 W/m^2 [31]
Glazing cover	Convection	T = 293 K, h = 5.7 W/(m^2· K) [38]
Ground	Adiabatic wall	q = 0 W/m^2
Other walls	Adiabatic wall	q = 0 W/m^2

2.4. Grid system and grid independence check

A structured grid is used in the computational domain to achieve high mesh quality and simulation accuracy, as shown in Fig. 2. Considering the effect of the boundary layer near the wall, the grids are densified. Other grids are more sparsely distributed to save the computational effort and reduce the computational time.

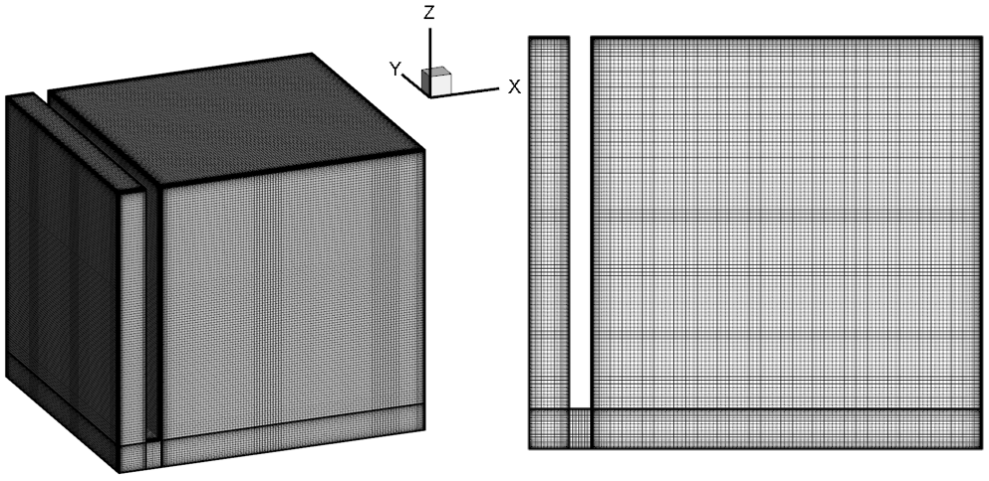

(a) (b)

Fig. 2. The grid system of the SC in buildings with PCR. (a) Global grid; (b) Front view of the grid

Three grid quantities of 1487632, 2508672, and 3645126 are considered for grid independence verification. SC models in buildings with PPCR or HPCR are calculated under uniform conditions, while the solar radiation is 500 W/m^2. The volume flow rate at the chimney outlet is monitored. The obtained results are shown in Table 2. The errors between the calculated volume flow rates for models with different grid numbers are within 3%, which indicates that the numerical results will not be significantly affected by a further increase in the grid numbers. Therefore, a model with a grid number of 2508672 is used in this study.

Table 2 Validation of grid independence.

Grid numbers	1487632	2508672	3645126
Volume flow rate of the SC in the building with PPCR (m^3/s)	0.3874	0.3868	0.3972
Volume flow rate of the SC in the building with HPCR (m^3/s)	0.2089	0.2150	0.2213

The computation is implemented using ANSYS Fluent 19.0. The SIMPLE algorithm is used for pressure-velocity coupling. The Green-Gauss node-based and PRESTO! method is applied for the gradient and pressure discretization. The second-order upwind method is used for all the other diffusion terms. The calculation is considered to converge until all the variable residuals are less than 10^{-5} and the volume flow rate at the chimney outlet remains constant.

2.5. Validation

The model is validated using the experimental data from Mathur et al. (Mathur et al., 2006). The set dimensions and boundary conditions of the model are similar to those of the experiment. The obtained results (absorbing wall height in the range of 0.7-0.9 m, air inlet size in the range of 0.1-0.3 m, flow channel width in the range of 0.1-0.2 m, and solar radiation of 500 W/m^2), are compared with the experimental results (Table 3). The relative error within 6% between the numerical results and the experimental results indicate that the numerical method and developed model are reliable.

Table 3 Comparison results with experimental data.

Case	Absorbing wall height (m)	Air inlet size (m)	Flow channel size (m)	Experimental ACH	Present ACH	Error
Case 1	0.9	0.1	0.1	2.40	2.47	2.92%
Case 2	0.9	0.1	0.2	2.00	2.12	6.00%
Case 3	0.8	0.2	0.1	2.93	2.78	5.12%
Case 4	0.8	0.2	0.2	4.26	3.79	5.80%
Case 5	0.7	0.3	0.1	4.00	3.84	4.00%
Case 6	0.7	0.3	0.2	5.20	4.94	5.10%

3. Results and discussion

In this section, the feasibility of combining SC with the photocatalytic technology is analyzed, and the overall performance of the systems under different geometrical parameters is evaluated. In addition, the structure of the SC with HPCR is optimized to obtain a high photocatalytic performance. The HPCR having a porosity in the range of 0.7-0.9 and a pore diameter of 6 mm, is positioned at 0.45 m above the ground inside the flow channel. The length of the reactor varies between 0.15 m and 2.4 m.

3.1. Ventilation performance of the SC with PCRs

Fig. 3 illustrates the velocity distribution in the y = 1.5 m plane of the SC with PCRs. It is evident that the air velocity in the flow channel exhibits a more uniformly distributed in the SC with PPCR because the reactor does not significantly affect the flow field. For the HPCR, the flow resistance increases, and the velocity decreases due to the porous media. In the SC with PPCR, the airflow in the flow channel reaches its maximum velocity at the chimney outlet close to the absorbing wall. Meanwhile, in the SC with HPCR, this occurs closer to the middle of the flow channel, adjacent to the absorbing wall. The presence of the HPCR increases the internal resistance, which weakens the upward driving force. As a consequence, the airflow velocity in the upper section of the chimney decelerates, owing to the inflow of exterior air from the chimney exit near the glass.

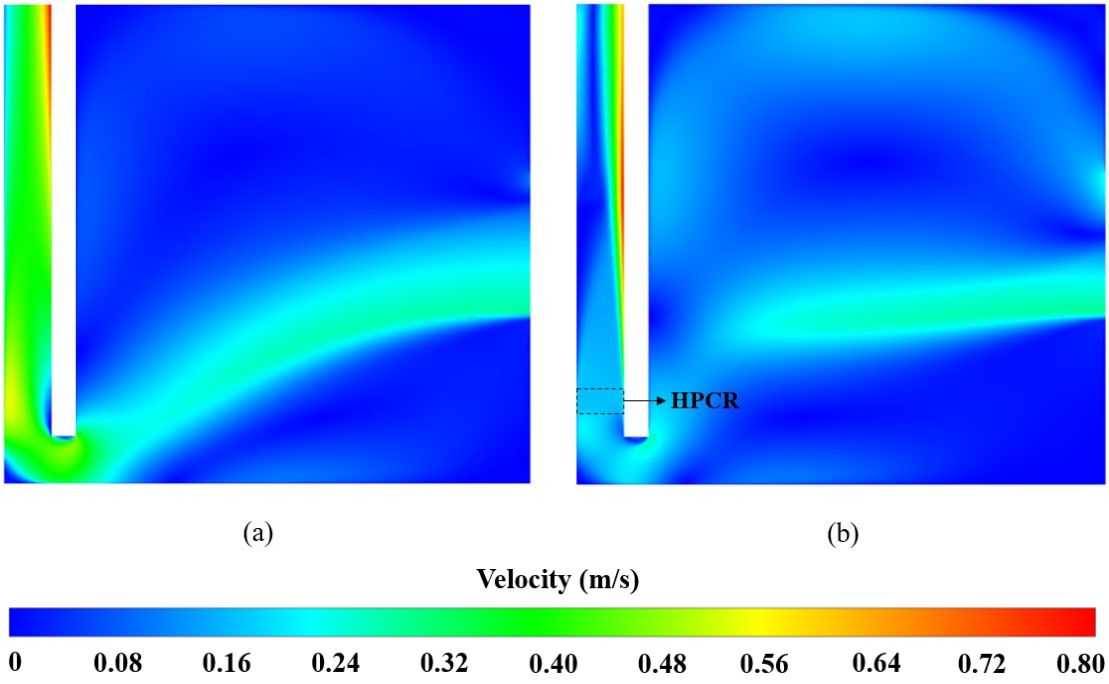

Fig.3. Velocity contours in the y = 1.5 m plane of the SC with PCRs. (a) SC with PPCR; (b) SC with HPCR.

Fig. 4 shows the fresh air flow rates of the SC with PPCR and HPCR. The fresh air rate for the SC with PPCR is approximately 1.34 times greater than for the SC with HPCR at a solar radiation of 1100 W/m^2. The porous media blocks the airflow, which restricts the room ventilation. Nevertheless, the indoor airflow organization will be optimized to enhance the indoor comfort by setting the HPCR, as shown in Fig. 3. Despite the reduction of the fresh air rate, SC with HPCR still meets the *ASHRAE 62.1-2016* fresh air standard (Standard, 2010). As the solar radiation intensifies, the temperature of the absorber wall rises, leading to increased indoor ventilation in both PCRs. The increase of the fresh air flow rate of the SC with PPCR is slightly more significant than that of the SC with HPCR. This difference can be attributed to the fact that the HPCR absorbs some energy and enhances the airflow resistance, as depicted in Figure 4.

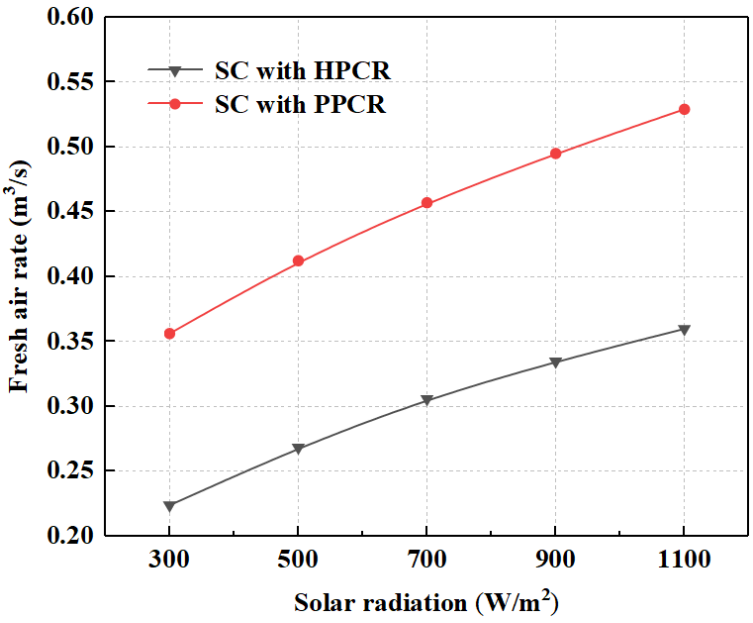

Fig.4. The fresh air flow rates of the SC with PCRs.

Fig. 5 shows the pressure distribution in the y = 1.5 m plane of the SC with PPCR and HPCR. The two systems have the same pressure distributions across the room: positive pressure at the top of the zone and negative pressure at its bottom. Due to the narrow chimney entrance of the SC with PPCR, the faster-moving air at the corner separates from the wall, and a maximum negative pressure value can be observed. For the SC with HPCR, the negative pressure continues to increase as the air enters the reactor due to the heightened resistance. However, as the air passes through the reactor, the pressure gradually recovers.

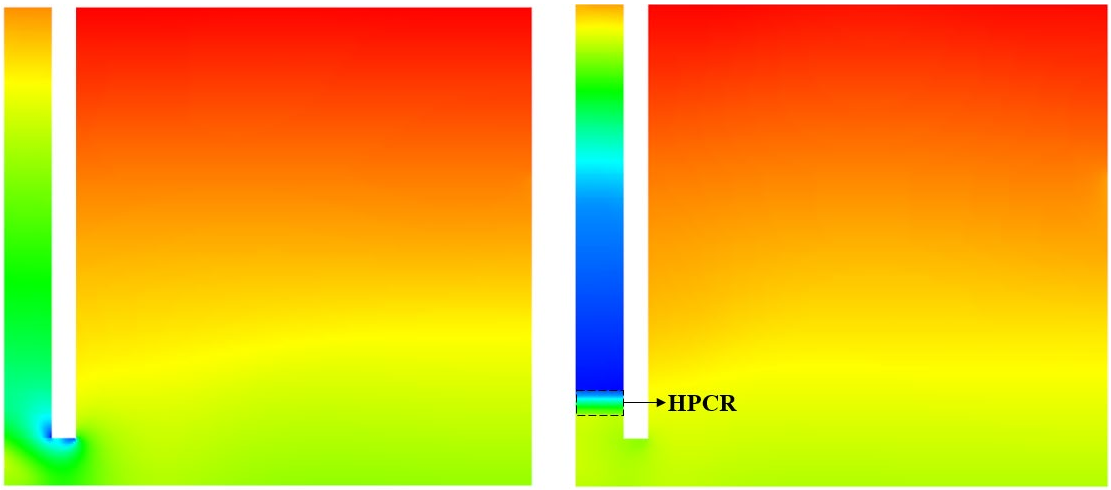

(a) (b)

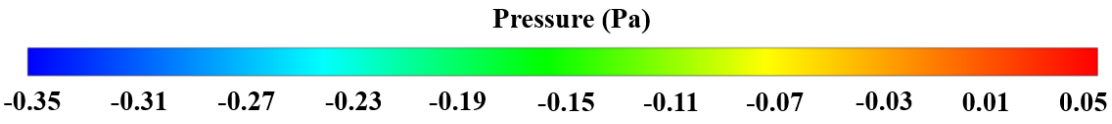

Fig.5. Pressure contours in the y = 1.5 m plane of the SC with PCRs. (a) SC with PPCR; (b) SC with HPCR.

3.2. Photocatalytic performance of the SC with PCRs

Fig. 6 shows the methane concentration distribution in the y = 1.5 m plane of the SC with PPCR and HPCR. It is evident that in the SC with PPCR, the methane concentration is higher at the inlet of the reactor, exhibiting a noticeable concentration gradient that gradually diminishes along the direction of flow. Due to the consistent airflow within the chimney, the higher methane concentration on the left side diffuses slowly towards the right side, resulting in a minor alteration in the methane concentration on the left side of the flow channel. In the SC with HPCR, the methane concentration is uniformly decreased to 1.69 ppm after the air enters the reactor. Due to the blockage of the porous media, the airflow lacks driving force, which leads to the increase of the methane concentration as outside air flows into the chimney and mixes with the purified air.

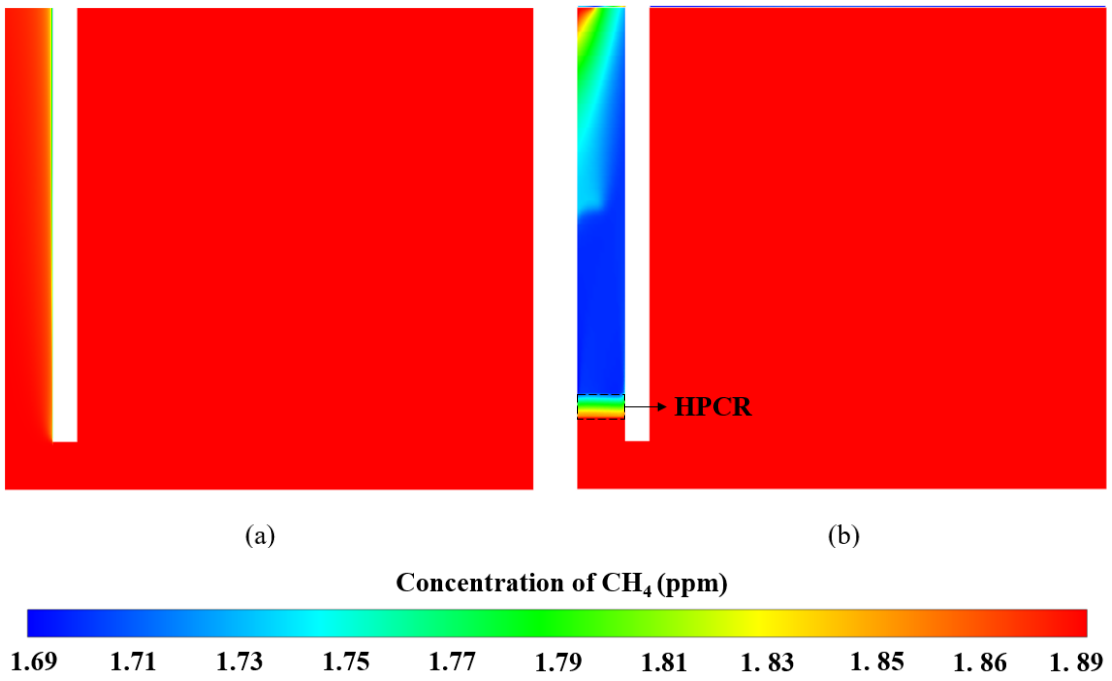

Fig.6. The methane concentration contours in the y = 1.5 m plane of the SC with

PCRs. (a) SC with PPCR; (b) SC with HPCR.

Fig. 7 shows the photocatalytic efficiency and the purification rate of methane in the SC with PCRs. It can be observed that the photocatalytic efficiency of the PPCR is considerably lower compared to that of the HPCR. The air in the SC with PPCR smoothly flows in the flow channel with low kinetic energy on the glass side, making it difficult for methane to diffuse to the catalytic layer. The airflow velocity in the flow channel reaches 0.35 m/s, resulting in a relatively short residence time for methane on the catalytic layer surface. In contrast, the HPCR has a larger reaction area and a longer methane residence time on the photocatalyst, which leads to a more thorough degradation.

The methane photocatalytic efficiency in the SC with PCRs can be enhanced by increasing the solar radiation. When the solar radiation increases from 300 W/m^2 to 1100 W/m^2, the airflow rate and the reaction rate of the methane photocatalysis increase. The photocatalytic efficiency and purification rate of methane in the SC with HPCR show an almost linear growth trend. For the SC with PPCR, the photocatalytic efficiency remains relatively stable as solar radiation increases, while the methane purification rate steadily increases. The methane purification rates of the SC with HPCR are 3.69 times, 3.43 times, and 2.99 times higher than those of the SC with PPCR under solar radiations of 1100 W/m^2, 700 W/m^2, and 300 W/m^2, respectively. The methane photocatalytic efficiency in the PPCR is noticeably lower compared to that in the HPCR, and the disparity between the two systems progressively widens with the increase of solar radiation.

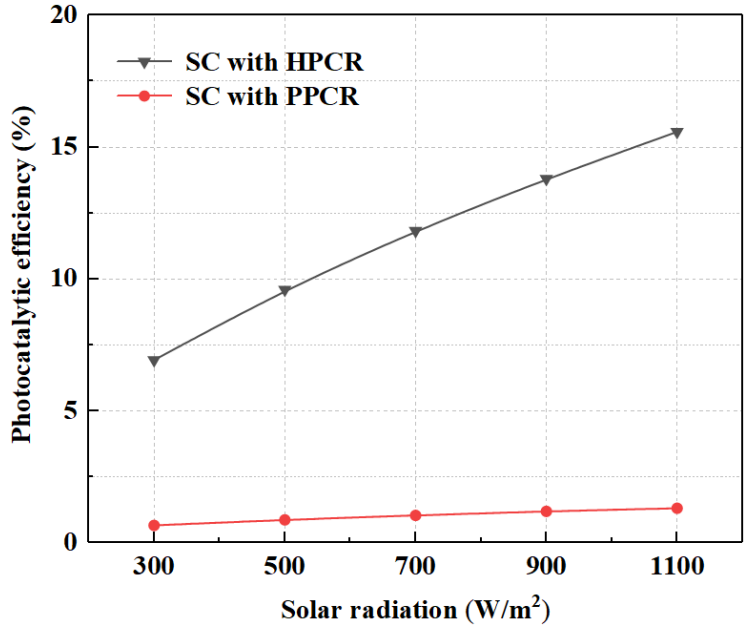

(a)

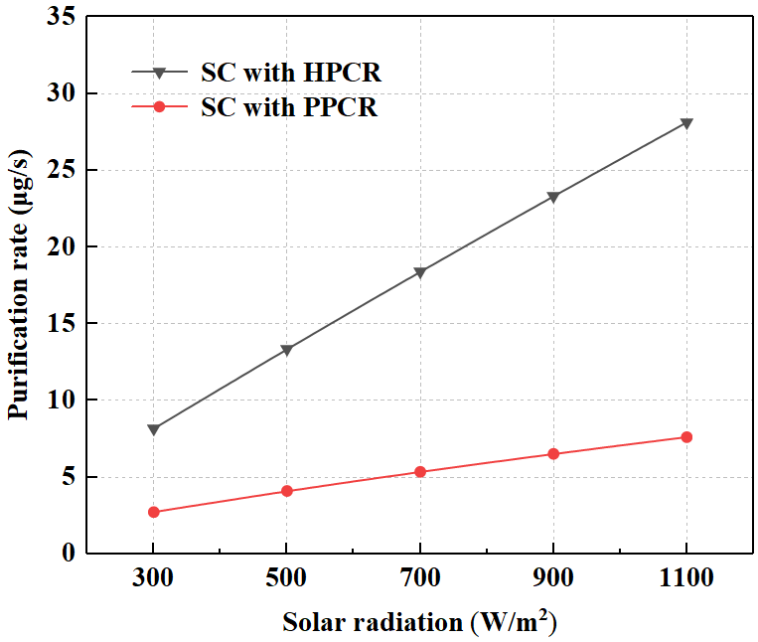

(b)

Fig.7. Effect of solar radiation on the methane removal performance of SC with PCRs. (a) the photocatalytic efficiency of methane; (b) the purification rate of methane

3.3. Structure optimization of the SC with HPCR

In terms of methane degradation, the SC with HPCR performs better than that with

PPCR and can satisfy the requirements of indoor ventilation. To study the impact of the length and porosity of the reactor as well as the flow channel width on the system performance, the SC with HPCR should be further investigated.

It can be seen from Fig. 8 that the indoor fresh air rate can be increased by widening the flow channel. The enlarged width of the flow channel decreases the internal friction loss and strengthens the driving force of the airflow. When the flow channel width increases from 0.1 m to 0.15 m, the fresh air rate increases more than the case where it increases from 0.25 m to 0.3 m. When the width reaches 0.25 m, the natural convection of air inside the channel becomes disorganized and the vortex impedes the airflow, slowing the growth of the fresh air rate. In addition, the airflow restriction caused by the porous media diminishes, and the flow loss decreases when the porosity increases.

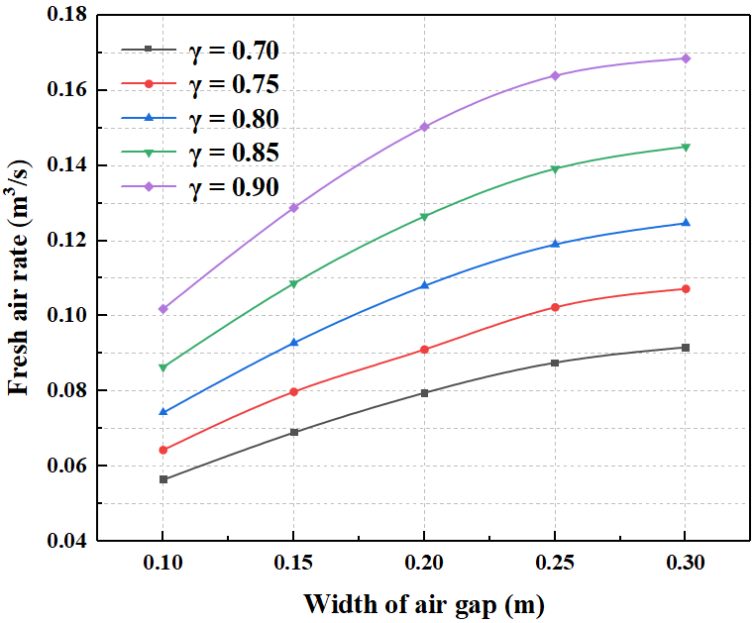

Fig.8. The fresh air rate of the SC with HPCR at G = 500 W/m^2, D_p = 6 mm.

Fig. 9 shows the methane concentration distributions of the SC with HPCR. It can be observed that fresh air flows through the HPCR, where the methane performs photocatalytic oxidation. As the methane concentration gradually decreases to a steady level, the degraded methane ascends and blends with the reverse flow. The air enters

the broader flow channel at a lower speed, providing methane with enough time to contact the reactor. Moreover, the wide flow channel provided by a larger reaction zone results in a higher methane degradation rate. Furthermore, the air near the glass receives less heat and driving force due to the broader flow channel, which makes the reflux phenomena more noticeable.

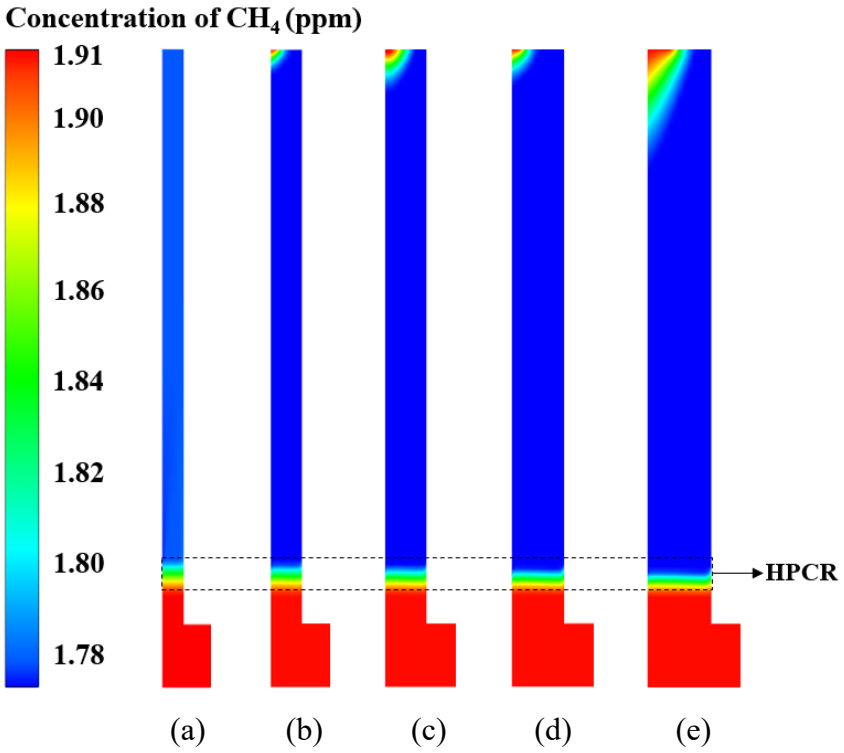

Fig.9. The methane concentration distributions in the y = 1.5 m plane at L = 0.15 m, D_p = 6 mm, γ = 0.8. (a) d = 0.10 m; (b) d = 0.15 m; (c) d = 0.20 m; (d) d = 0.25 m; (e) d = 0.30 m.

Fig. 10 illustrates the impact of the flow channel width and porosity of the HPCR on the methane photocatalysis performance. It can be seen that the methane photocatalytic efficiency significantly increases when the flow channel is wider. This tendency is clearer for the SC with HPCR of smaller porosity. When the flow channel width increases from 0.1 m to 0.3 m, the methane photocatalytic efficiency for the SC with HPCR at γ= 0.9 increases from 2.16% to 3.63%, while the methane photocatalytic efficiency for the SC with HPCR at γ = 0.7 increases from 12.05% to 18.80%. When the porosity decreases, the influence of the channel width on the

methane photocatalytic efficiency becomes more noticeable.

Similarly, widening the flow channel can significantly increase the methane purification rate at a certain porosity. It can be clearly seen that increasing the flow channel width within a specific range will increase the fresh air rate. The methane purification rate significantly increases due to the simultaneous increase of the fresh air rate and the methane photocatalytic efficiency. In addition, increasing the porosity of the reactor can result in increasing the methane purification rate. When the porosity is smaller, the methane purification rate more rapidly increases with the widening of the flow channel.

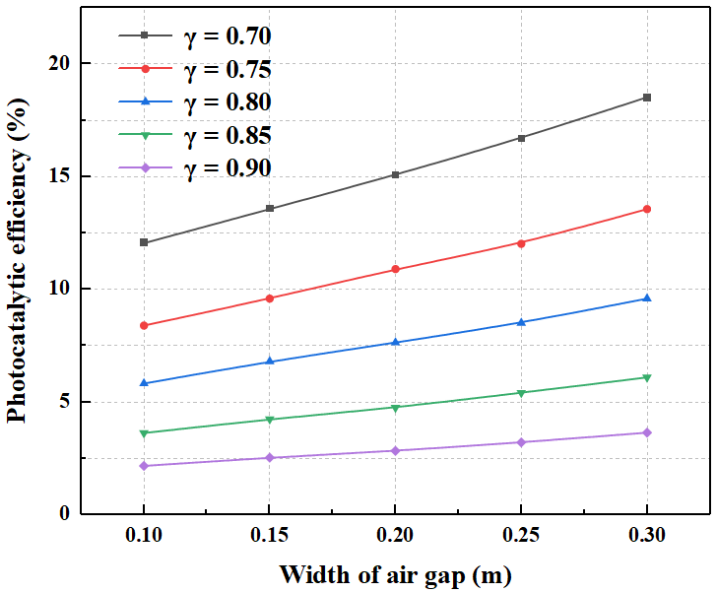

(a)

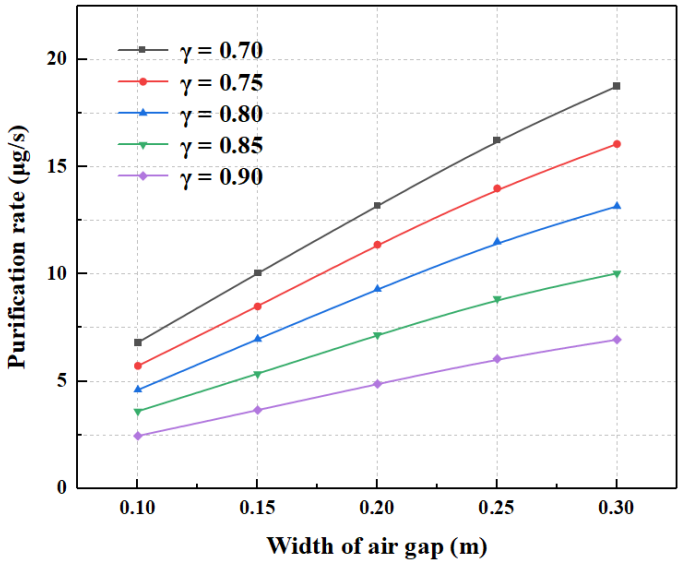

(b)

Fig.10. Effect of the air gap width on the methane removal performance at G = 500 W/m^2, D_p = 6 mm. (a) methane photocatalytic efficiency; (b) methane purification rate.

3.4. Reactor optimization of the SC with HPCR

As previously mentioned in section 3.3, the SC has high methane removal performance with a flow channel of 0.3 m. However, the backflow phenomenon is clear and affects the indoor ventilation. To minimize the backflow and optimize the ventilation efficiency, a non-reactive porous media zone having a size of 0.3 m × 3 m × 0.15 m and a porosity of 0.8 is installed at the chimney outlet of the flow channel.

Fig. 11 shows the fresh air rate of the SC with HPCR. The fresh air volume rate steadily decreases when the length of HPCR and the airflow resistance increase. With a smaller porosity at an HPCR length in the range of 0.15-1.65 m, the fresh air rate is lower.

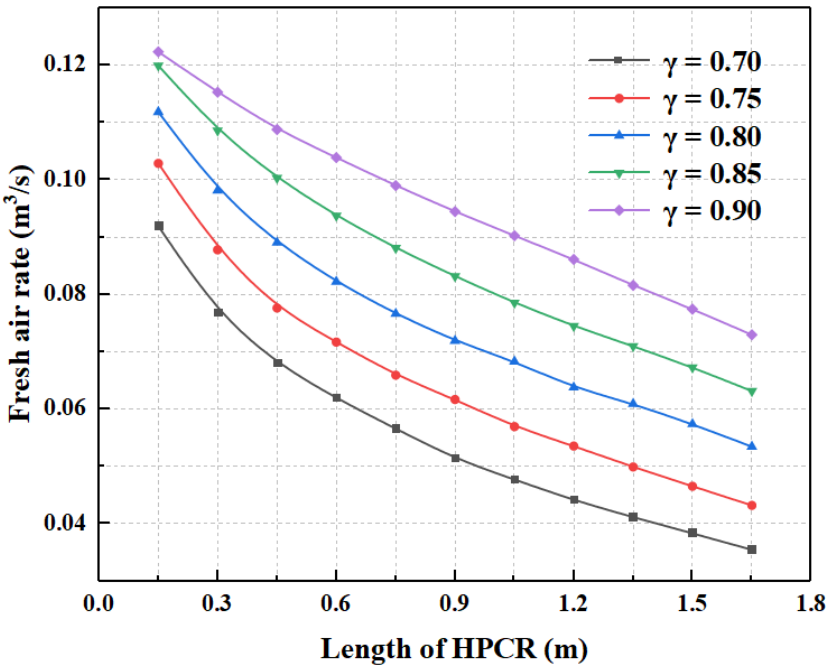

Fig.11. The fresh air rate of the SC with HPCR at G = 500 W/m^2, D_p = 6 mm.

Fig. 12 shows the methane concentration distributions in the y = 1.5 m plane of

462 the SC with HPCR. The methane concentration gradient flowing through the reactor
463 gradually decreases with the increase of the HPCR porosity, and the methane
464 degradation performance then decreases. This is due to the fact that a smaller porosity
465 reactor can provide a broader reaction area and longer reaction time for the methane
466 photocatalytic reaction.

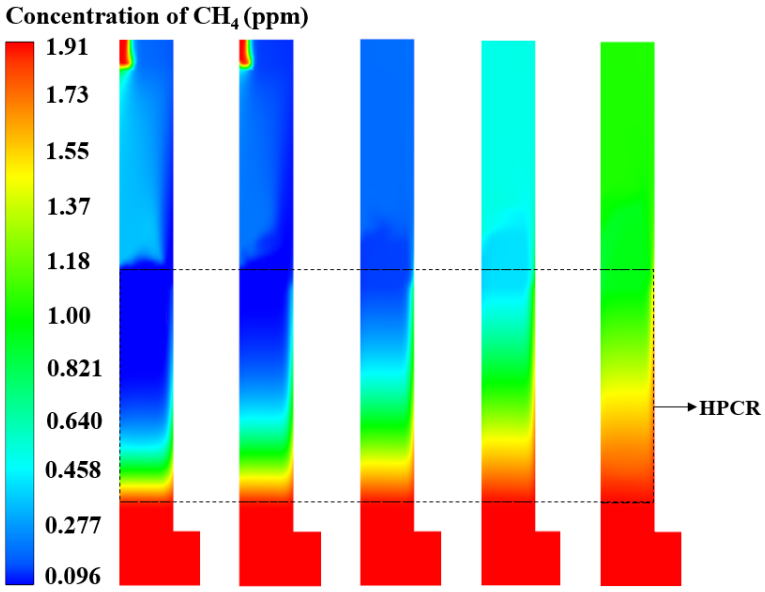

467
468

469 Fig.12. Methane concentration distributions in the y = 1.5 m plane of the SC with
470 HPCR at L = 1.2 m, D_p = 6 mm. (a) γ = 0.70; (b) γ = 0.75; (c) γ = 0.80; (d) γ = 0.85;
471 (e) γ = 0.90.
472

473 Fig. 13 shows the methane photocatalytic efficiency in the SC with HPCR. It can
474 be seen that the increased length of the reactor expands the reaction area, extends the
475 reaction time, and effectively improves the methane photocatalytic efficiency. The
476 increase of the methane photocatalytic efficiency is significant at first, and then
477 approaches a flat trend. At a smaller porosity, the methane photocatalytic efficiency
478 increases faster and levels off earlier.

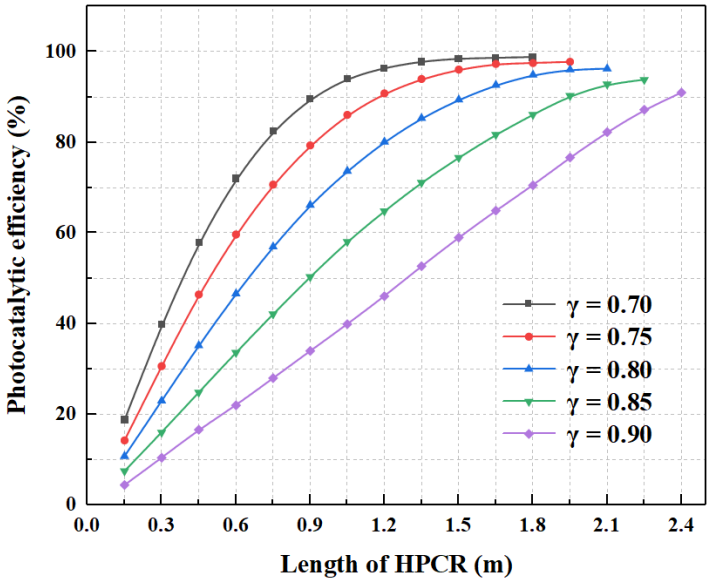

Fig.13. The methane photocatalytic efficiency in the SC with HPCR at G = 500 W/m^2, D_p = 6 mm.

It can be seen from Fig. 14 that the methane purification rate in the SC with HPCR first increases and then decreases with the increase of the reactor length. When the porosity of the HPCR is 0.7, a gradual increase in the length of the HPCR from 0.05 m to 1.35 m leads to a significant increase in the methane photocatalytic efficiency, which outweighs the impact of flow loss. When the length of the HPCR is extended from 1.35 m to 2.1 m, there is a slight enhancement in methane photocatalytic efficiency. However, the flow rate experiences a continued decrease, which predominantly influences the decline in methane degradation. On the other hand, as the porosity increases, the length of the HPCR associated with the maximum methane purification rate progressively lengthens. The maximum methane purification rate is reached for the systems with γ = 0.7, 0.75, 0.8, 0.85, and 0.9 at HPCR lengths of 0.65 m, 0.9 m, 1.35 m, 1.5 m, and 1.95 m, respectively. The methane purification rate in the SC with HPCR reaches an optimum value of 57.27 μ g/s at γ = 0.85 and L = 1.5 m.

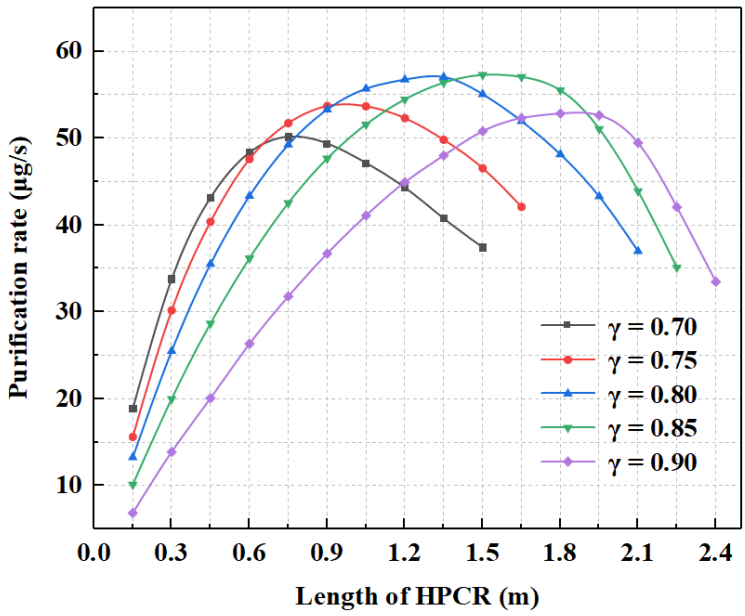

Fig.14. The methane purification rate in the SC with HPCR at G = 500 W/m^2, D_p = 6 mm.

4. Conclusions

In this study, a small-scale SC in buildings integrated with PCRs is proposed to perform indoor ventilation and atmospheric methane degradation. The factors affecting the indoor ventilation and methane removal performance of the proposed system are analyzed through numerical simulations. The following conclusions can be drawn:

(1) The methane removal performance of SC in buildings with HPCR is 3.69 times higher than that with PPCR under solar radiation of 1100 W/m^2, provided that the ventilation requirements are met. When the reaction zone length increases, the methane photocatalytic efficiency gradually increases, and the methane will finally entirely degrade.

(2) When the air gap width and solar radiation increase, the methane removal and ventilation performance of the SC in buildings with HPCR are improved. When the air gap width increases, the photocatalytic reaction time is prolonged due to the increased air rate and slower air flow. When the solar radiation intensity increases, the increased driving force of the upward flow and the accelerated photocatalytic reaction rate enhance the methane removal performance. The optimum value of the purification rate

is 57.27 μg/s at $\gamma = 0.85$ and $L = 1.5$ m under a solar radiation of 500 W/m^2.

(3) The backflow phenomenon appears at the exit of the flow channel due to the increase of the airflow resistance in it. In addition, the backflow is weakened, and the performance of methane degradation can be ensured by placing a tiny patch of porous material near the chimney outlet.

Acknowledgments

This research was supported by the National Key Research and Development Plan (Grant No. 2019YFE0197500), the European Commission H2020 Marie Curie Research and Innovation Staff Exchange (RISE) award (Grant No. 871998), the National Natural Science Foundation of China (Grant No. 52278123), and the Fundamental Research Funds for the Central Universities (Grant No. 225206002).

References

Arce, J., Jiménez, M., Guzmán, J., Heras, M., Alvarez, G., Xamán, J., 2009. Experimental study for natural ventilation on a solar chimney. Renewable Energy 34(12), 2928-2934.

Bassiouny, R., Koura, N.S., 2008. An analytical and numerical study of solar chimney use for room natural ventilation. Energy and buildings 40(5), 865-873.

Burek, S., Habeb, A., 2007. Air flow and thermal efficiency characteristics in solar chimneys and Trombe Walls. Energy and buildings 39(2), 128-135.

Chen, X., Li, Y., Pan, X., Cortie, D., Huang, X., Yi, Z., 2016. Photocatalytic oxidation of methane over silver decorated zinc oxide nanocatalysts. Nat Commun 7(1), 12273.

Ganesan, A.L., Schwietzke, S., Poulter, B., Arnold, T., Lan, X., Rigby, M., Vogel, F.R., Werf, G.R., Janssens‐Maenhout, G., Boesch, H., Pandey, S., Manning, A.J., Jackson, R.B., Nisbet, E.G., Manning, M.R., 2019. Advancing Scientific Understanding of the Global Methane Budget in Support of the Paris Agreement. Global Biogeochemical Cycles 33(12), 1475-1512.

Haeger, A., Kleinschmidt, O., Hesse, D., 2004. Kinetics of photocatalyzed gas reactions using titanium dioxide as the catalyst part II: Photocatalyzed total oxidation of alkanes with oxygen. Chemical Engineering & Technology: Industrial Chemistry‐Plant Equipment‐Process Engineering‐Biotechnology 27(9), 1019-1026.

Harmsen, M., van Vuuren, D.P., Bodirsky, B.L., Chateau, J., Durand-Lasserve, O., Drouet, L., Fricko, O., Fujimori, S., Gernaat, D.E.H.J., Hanaoka, T., Hilaire, J., Keramidas, K., Luderer, G., Moura, M.C.P., Sano, F., Smith, S.J., Wada, K., 2019. The role of methane in future climate strategies: mitigation potentials and climate impacts. Climatic Change 163(3), 1409-1425.

Hepburn, C., Adlen, E., Beddington, J., Carter, E.A., Fuss, S., Mac Dowell, N., Minx, J.C., Smith, P., Williams, C.K., 2019. The technological and economic prospects for CO2 utilization and removal. Nature 575(7781), 87-97.

Hoegh-Guldberg, O., Jacob, D., Taylor, M., Guillén Bolaños, T., Bindi, M., Brown, S., Camilloni, I.A., Diedhiou, A., Djalante, R., Ebi, K., 2019. The human imperative of stabilizing global climate change at 1.5 °C. Science 365(6459), eaaw6974.

Huang, Y., Shao, Y., Bai, Y., Yuan, Q., Ming, T., Davies, P., Lu, X., De Richter, R., Li, W., 2021. Feasibility of Solar Updraft Towers as Photocatalytic Reactors for Removal of Atmospheric Methane–The Role of Catalysts and Rate Limiting Steps. Frontiers in chemistry 9, 745347.

Jackson, R.B., Saunois, M., Bousquet, P., Canadell, J.G., Poulter, B., Stavert, A.R., Bergamaschi, P., Niwa, Y., Segers, A., Tsuruta, A., 2020. Increasing anthropogenic methane emissions arise equally from agricultural and fossil fuel sources. Environmental Research Letters 15(7), 071002.

Jackson, R.B., Solomon, E.I., Canadell, J.G., Cargnello, M., Field, C.B., 2019. Methane removal and atmospheric restoration. Nature Sustainability 2(6), 436-438.

Jeffrey, L.C., Maher, D.T., Chiri, E., Leung, P.M., Nauer, P.A., Arndt, S.K., Tait, D.R.,

Greening, C., Johnston, S.G., 2021. Bark-dwelling methanotrophic bacteria decrease methane emissions from trees. Nat Commun 12(1), 2127.
Keramidas, K., Fosse, F., Diaz Vazquez, A., Dowling, P., Garaffa, R., Després, J., Russ, H.P., Schade, B., Schmitz, A., Soria Ramirez, A., 2021. Global Energy and Climate Outlook 2021: advancing towards climate neutrality. Luxembourg: Publications Office of the European Union.
Li, Z., Pan, X., Yi, Z., 2019. Photocatalytic oxidation of methane over CuO-decorated ZnO nanocatalysts. Journal of Materials Chemistry A 7(2), 469-475.
Liu, G., Peng, S., Lin, X., Ciais, P., Li, X., Xi, Y., Lu, Z., Chang, J., Saunois, M., Wu, Y., 2021. Recent slowdown of anthropogenic methane emissions in China driven by stabilized coal production. Environmental Science & Technology Letters 8(9), 739-746.
Lustemberg, P.G., Palomino, R.M., Gutiérrez, R.n.A., Grinter, D.C., Vorokhta, M., Liu, Z., Ramírez, P.J., Matolín, V., Ganduglia-Pirovano, M.V.n., Senanayake, S.D., 2018. Direct conversion of methane to methanol on Ni-Ceria surfaces: metal–support interactions and water-enabled catalytic conversion by site blocking. Journal of the American Chemical Society 140(24), 7681-7687.
Mathur, J., Bansal, N., Mathur, S., Jain, M., 2006. Experimental investigations on solar chimney for room ventilation. Solar Energy 80(8), 927-935.
Mazumder, S., Sengupta, D., 2002. Sub-grid scale modeling of heterogeneous chemical reactions and transport in full-scale catalytic converters. Combustion and flame 131(1-2), 85-97.
Meng, X., Cui, X., Rajan, N.P., Yu, L., Deng, D., Bao, X., 2019. Direct Methane Conversion under Mild Condition by Thermo-, Electro-, or Photocatalysis. Chem 5(9), 2296-2325.
Ming, T., Davies, P., Liu, W., Caillol, S., 2017. Removal of non-CO2 greenhouse gases by large-scale atmospheric solar photocatalysis. Progress in Energy and Combustion Science 60, 68-96.
Ming, T., Gui, H., Shi, T., Xiong, H., Wu, Y., Shao, Y., Li, W., Lu, X., de Richter, R., 2021. Solar chimney power plant integrated with a photocatalytic reactor to remove atmospheric methane: A numerical analysis. Solar Energy 226, 101-111.
Ming, T., Xiong, H., Shi, T., Wu, Y., Wang, C., Wen, Y., Li, W., de Richter, R., Zhou, N., 2022. A novel green technology: Reducing carbon dioxide and eliminating methane from the atmosphere. International Journal of Energy Research 46(14), 20107-20120.
Ocko, I.B., Naik, V., Paynter, D., 2018. Rapid and reliable assessment of methane impacts on climate. Atmospheric Chemistry and Physics 18(21), 15555-15568.
Ocko, I.B., Sun, T., Shindell, D., Oppenheimer, M., Hristov, A.N., Pacala, S.W., Mauzerall, D.L., Xu, Y., Hamburg, S.P., 2021. Acting rapidly to deploy readily available methane mitigation measures by sector can immediately slow global warming. Environmental Research Letters 16(5), 054042.
Ong, K., Chow, C., 2003. Performance of a solar chimney. Solar energy 74(1), 1-17.
Pan, X., Chen, X., Yi, Z., 2016. Photocatalytic oxidation of methane over SrCO 3 decorated SrTiO 3 nanocatalysts via a synergistic effect. Physical Chemistry Chemical

611 Physics 18(46), 31400-31409.
612 Pörtner, H.-O., Roberts, D.C., Adams, H., Adler, C., Aldunce, P., Ali, E., Begum, R.A.,
613 Betts, R., Kerr, R.B., Biesbroek, R., 2022. Climate change 2022: Impacts, adaptation
614 and vulnerability. IPCC Sixth Assessment Report.
615 Rabani, M., Kalantar, V., Dehghan, A.A., Faghih, A.K., 2015. Empirical investigation
616 of the cooling performance of a new designed Trombe wall in combination with solar
617 chimney and water spraying system. Energy and Buildings 102, 45-57.
618 Saunois, M., Jackson, R.B., Bousquet, P., Poulter, B., Canadell, J.G., 2016. The growing
619 role of methane in anthropogenic climate change. Environmental Research Letters
620 11(12), 120207.
621 Saunois, M., Stavert, A.R., Poulter, B., Bousquet, P., Canadell, J.G., Jackson, R.B.,
622 Raymond, P.A., Dlugokencky, E.J., Houweling, S., Patra, P.K., 2020. The global
623 methane budget 2000–2017. Earth system science data 12(3), 1561-1623.
624 Saunois, M., Stavert, A.R., Poulter, B., Bousquet, P., Zhuang, Q., 2020. The Global
625 Methane Budget 2000–2017. Earth System Science Data 12(3), 1561-1623.
626 Shi, L., Zhang, G., Cheng, X., Guo, Y., Wang, J., Chew, M.Y.L., 2016. Developing an
627 empirical model for roof solar chimney based on experimental data from various test
628 rigs. Building and Environment 110, 115-128.
629 Shi, L., Zhang, G., Yang, W., Huang, D., Cheng, X., Setunge, S., 2018. Determining the
630 influencing factors on the performance of solar chimney in buildings. Renewable and
631 Sustainable Energy Reviews 88, 223-238.
632 Song, H., Meng, X., Wang, Z., Liu, H., Ye, J., 2019. Solar-Energy-Mediated Methane
633 Conversion. Joule 3(7), 1606-1636.
634 Standard, A., 2010. 62: Ventilation for Acceptable Indoor Air Quality American Society
635 of Heating. Refrigeration and Air-Conditioning Engineers, Inc., Atlanta, GA.
636 Wada, K., Yoshida, K., Takatani, T., Watanabe, Y., 1993. Selective photo-oxidation of
637 light alkanes using solid metal oxide semiconductors. Applied Catalysis A: General
638 99(1), 21-36.
639 Wang, Q., Xiong, H., Ming, T., 2022. Methods of Large-Scale Capture and Removal of
640 Atmospheric Greenhouse Gases. Energies, p. 6560.
641 Wang, X., Tan, X., Yu, T., 2014. Modeling of formaldehyde photocatalytic degradation
642 in a honeycomb monolith reactor using computational fluid dynamics. Industrial &
643 Engineering Chemistry Research 53(48), 18402-18410.
644 Wu, S.Y., Xu, L., Xiao, L., 2020. Air purification and thermal performance of
645 photocatalytic-Trombe wall based on multiple physical fields coupling. Renewable
646 Energy 148, 338-348.
647 Xiong, H., Ming, T., Wu, Y., Wang, C., Chen, Q., Li, W., Mu, L., de Richter, R., Yuan,
648 Y., 2022. Numerical analysis of solar chimney power plant integrated with CH4
649 photocatalytic reactors for fighting global warming under ambient crosswind.
650 Renewable Energy 201, 678-690.
651 Yu, B., He, W., Li, N., Zhou, F., Shen, Z., Chen, H., Xu, G., 2017. Experiments and
652 kinetics of solar PCO for indoor air purification in PCO/TW system. Building and

Environment 115, 130-146.
Yu, B., Hou, J., He, W., Liu, S., Hu, Z., Ji, J., Chen, H., Xu, G., 2018. Study on a high-performance photocatalytic-Trombe wall system for space heating and air purification. Applied energy 226, 365-380.
Zhang, J., Wang, Y., Wang, Y., Bai, Y., Feng, X., Zhu, J., Lu, X., Mu, L., Ming, T., de Richter, R., Li, W., 2022. Solar Driven Gas Phase Advanced Oxidation Processes for Methane Removal - Challenges and Perspectives. Chemistry, e202201984.
Zhu, W., Shen, M., Fan, G., Yang, A., Meyer, J.R., Ou, Y., Yin, B., Fortner, J., Foston, M., Li, Z., Zou, Z., Sadtler, B., 2018. Facet-Dependent Enhancement in the Activity of Bismuth Vanadate Microcrystals for the Photocatalytic Conversion of Methane to Methanol. ACS Applied Nano Materials 1(12), 6683-6691.